J Adv Ceram

Research Article

Temperature-modulated high-entropy perovskite cathodes with superior electrocatalytic activity for reversible solid oxide cells

Jiahui Zhu[1], Xiaofei Zhu[1,✉], Yinlin Chang[2], Zetian Tao[2,✉], Haocong Wang[3], Wenwen Zhang[4], Defeng Zhou[1], Jinghe Bai[1,✉]

Cite this article: Zhu J, Zhu X, Chang Y, et al. *J Adv Ceram* 2026, **15**: 9221315. https://doi.org/10.26599/JAC.2026.9221315

ABSTRACT: Solid oxide cells (SOCs) hold great promise for clean energy conversion, yet conventional cathodes such as $La_{0.6}Sr_{0.4}Co_{0.2}Fe_{0.8}O_{3-\delta}$ (LSCF) suffer from insufficient electrocatalytic activity and poor CO_2 tolerance. This study designed a high-entropy perovskite, $La_{0.2}Sr_{0.2}Pr_{0.2}Nd_{0.2}Ba_{0.2}Co_{0.2}Fe_{0.8}O_{3-\delta}$ (HELSCF), via A-site high-entropy modification of LSCF. By regulating the synthesis temperature, two distinct crystal structures were achieved: an asymmetric tetragonal phase (HELSCF-*Pbnm*) with enhanced lattice distortion obtained at 1000 °C and a symmetric cubic phase (HELSCF-*Pm*3*m*) obtained at 1100 °C. Comprehensive characterizations confirmed that HELSCF-*Pbnm* exhibits superior properties, including a higher specific surface area, increased oxygen vacancy concentration, and optimized electronic structure. At 750 °C, the HELSCF-*Pbnm*-based symmetric cell delivers the lowest area-specific resistance of 0.040 Ω·cm², along with excellent bifunctional activity toward both the oxygen reduction reaction and oxygen evolution reaction, as well as outstanding tolerance under CO_2-containing atmospheres. When employed as the cathode in a single cell, it achieves a maximum power density of up to 1.38 W·cm⁻², approximately 1.7 times that of LSCF. Furthermore, it demonstrates exceptional operational stability for over 260 h at 600 °C. Density functional theory calculations further reveal that the orthorhombic structure enhances O_2 adsorption and d–p orbital hybridization, synergistically boosting catalytic performance. A temperature-modulated high-entropy strategy offers a facile and effective route for developing high-performance, CO_2-tolerant cathodes for reversible SOCs.

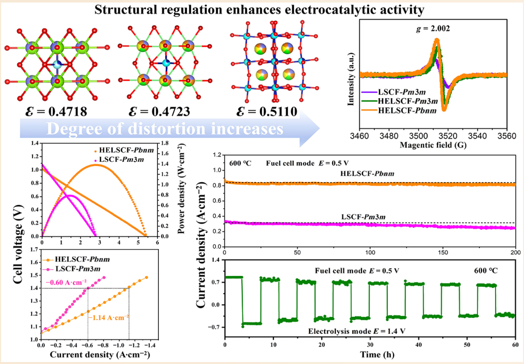

KEYWORDS: solid oxide cell (SOC); electrode; high-entropy perovskite; electrocatalytic activity; CO_2 tolerance

1 Introduction

The energy crisis and environmental issues are driving the development of high-efficiency and clean power generation technologies. Solid oxide cells (SOCs) have emerged as highly promising energy devices, as they can directly convert the chemical energy of fuels into electrical energy without being limited by the Carnot cycle [1]. However, excessively high operating temperatures have hindered their commercialization progress [2]. When the operating temperature is reduced, the core performance of SOCs relies heavily on cathode materials, which must possess both high oxygen reduction reaction (ORR) activity and stability [3,4].

ABO_3-type perovskites have emerged as one of the most promising electrode materials for intermediate-temperature SOCs (IT-SOCs) due to their comprehensive advantages that address the core requirements of high-temperature electrochemical reactions: their unique crystal structure allows flexible cation substitution or doping at both A-sites (rare-earth or alkaline-earth metals) and B-sites (transition metals), enabling precise regulation of oxygen vacancy concentration, electronic/ionic conductivity, and metal–oxygen bond strength to optimize ORR at cathodes or fuel oxidation kinetics at anodes; as a classic ABO_3-type perovskite, $La_{0.6}Sr_{0.4}Co_{0.2}Fe_{0.8}O_{3-\delta}$ (LSCF) possesses mixed ionic–electronic conductivity, enabling the simultaneous transport of oxygen ions and electrons [5]. It has thus become one of the most

---

[1] School of Chemistry and Life Science, Changchun University of Technology, Changchun 130012, China. [2] School of Resources, Environment and Safety Engineering, University of South China, Hengyang 421001, China. [3] State Key Laboratory of Rare Earth Resource Utilization, Changchun Institute of Applied Chemistry, Chinese Academy of Sciences, Changchun 130022, China. [4] State Key Laboratory of Catalysis, Dalian National Laboratory for CleanEnergy, Dalian Institute of Chemical Physics, Chinese Academy of Sciences, Dalian 116023, China.

✉ Corresponding authors. E-mail: X. Zhu, zhuxiaofei@ccut.edu.cn; Z. Tao, newton@mail.ustc.edu.cn, taozetian@usc.edu.cn; J. Bai, baijinghe95@126.com

Received: March 15, 2026; Revised: April 28, 2026; Accepted: May 2, 2026

extensively studied cathode materials for SOCs. However, LSCF still faces numerous challenges: its electrocatalytic activity fails to meet commercial requirements, and the alkaline earth metal ions it contains are prone to "poisoning" in CO_2 atmospheres, leading to irreversible performance degradation [6,7].

In recent years, high-entropy perovskites (HEPs) have garnered widespread attention in the field of energy materials [8–10]. The practical application potential of HEPs fundamentally relies on the rational stoichiometric design of multiple components and the efficient synergy of local structural regulation [11]. Compared with the conventional single-element doping strategy, the high-entropy design can significantly elevate the configurational entropy to above $1.5R$ while preserving the single-phase perovskite structure, simultaneously offering a new degree of freedom for precisely tuning defect distribution, maintaining continuous phase boundaries, and optimizing kinetic transport pathways. Furthermore, high-entropy engineering, driven by the disparities in atomic radii and electronegativities among multiple elements, induces pronounced lattice distortion. Such a highly distorted lattice substantially raises the energy barrier for atomic migration, thereby stabilizing the phase structure of the material. This mixing effect stems from the synergistic interactions of multiple elements across different structural scales, ultimately endowing the material with superior comprehensive performance [12]. The lattice distortion induced by the multimetal cation design in HEPs is conducive to increasing the oxygen vacancy concentration and regulating the electronic structure, which are key factors determining the kinetics of the ORR [13,14]. Notably, common ABO_3-type HEPs possess two distinct crystal structures: the symmetric cubic *Pm*3*m* structure and the asymmetric orthorhombic *Pbnm* structure, which exhibit significant differences in symmetry and lattice distortion [15,16]. Studies by Weng *et al.* [17] have shown that in highly symmetric perovskite systems, ionic doping induces bond angle distortion in the symmetric structure, endowing the perovskite with more active B-site oxygen ions and abundant oxygen vacancies during the ORR. Lattice distortion helps optimize the reaction energy barrier for the electrocatalytic activity of perovskites, and the degree of distortion is positively correlated with the electrocatalytic activity. Studies by Zou *et al.* [13] have shown that HEPs engineered with A-site high-entropy modification can finely tailor the electronic structure, oxygen vacancy formation, and ion transport pathways within the perovskite lattice by regulating the degree of octahedral distortion and bond angles. Combined with density functional theory (DFT) calculations, it has been confirmed that the distortion of BO_6 octahedra induced by the high-entropy effect shifts the center of the O 2p spectrum of the perovskite anode toward the Fermi level, thereby activating lattice oxygen and accelerating oxygen ion transport, which is conducive to enhancing the oxygen evolution reaction (OER) activity of the perovskite. Numerous previous studies have also demonstrated that HEPs cannot only enhance the electrocatalytic performance of materials but also suppress the segregation of alkaline-earth metal cations under CO_2 or Cr vapor environments, thereby improving the stability of electrodes under various poisoning atmospheres [18,19].

Overall, the lattice distortion induced by A-site high-entropy engineering of perovskites helps optimize the crystal structure, facilitate the formation of oxygen vacancies and suppress the segregation of alkaline-earth metals, thereby enhancing the electrocatalytic activity and CO_2 tolerance of perovskite materials when employed as SOC electrodes. Existing research has paid scant attention to the intricate correlations between the different structural symmetries of isocompositional HEPs, lattice distortion, oxygen vacancy generation, and electrocatalytic performance. For ABO_3-type HEPs, the entropy stabilization and local disorder induced by multicomponent occupation enable the construction of windows with different symmetries. The calcination temperature is one of the most critical steps in the material crystallization process [20,21], and thus, temperature regulation has the potential to serve as a simple and effective means of tuning HEPs into different structural states.

In this study, we adopted LSCF as the basic research model and synthesized two types of $La_{0.2}Sr_{0.2}Pr_{0.2}Nd_{0.2}Ba_{0.2}Co_{0.2}Fe_{0.8}O_{3-\delta}$ (HELSCF) by regulating the calcination temperature, namely, HELSCF-*Pm*3*m* with a symmetric *Pm*3*m* crystal structure and HELSCF-*Pbnm* with an asymmetric *Pbnm* crystal structure. Systematic experiments were conducted to investigate the structure-activity relationship between crystal symmetry, lattice distortion degree, oxygen vacancy concentration, and electrocatalytic activity of HELSCF when serving as an electrode for R-SOCs. Meanwhile, combined with DFT calculations, we performed an in-depth analysis of how the distortion degree and symmetry of HEPs affect their catalytic activity toward the ORR and OER. This study not only enables us to analyze the electrocatalytic performance of HEPs as R-SOC electrodes from the perspective of crystal structure but also provides novel design insights for preparing HEP materials with excellent electrocatalytic activity via the facile method of temperature regulation.

2 Experimental methods

2.1 Preparation of electrolytes and cathodes

All materials involved in this study were prepared via the sol–gel method. $La(NO_3)_3·6H_2O$, $Sr(NO_3)_2$, $Nd(NO_3)_3·6H_2O$, $Pr(NO_3)_3·H_2O$, $Ba(CH_3COO)_2$, $Co(NO_3)_2·6H_2O$, and $Fe(NO_3)_3·9H_2O$ were accurately weighed in stoichiometric ratios and dissolved in deionized water. Subsequently, citric acid and polyethylene glycol were added, and the mixture was continuously stirred at room temperature for 15 h to ensure uniform mixing of all components. The mixed solution was then transferred to a water bath for heating and evaporation to obtain an orange dry gel. Further heating was applied to induce self-combustion of the dry gel, and the resulting brown powder was collected. The obtained brown powder was precalcined at 650 °C for 5 h, followed by calcination at 1000 and 1100 °C for 5 h to obtain the target materials HELSCF-*Pbnm* and HELSCF-*Pm*3*m*, respectively.

2.2 Assemble symmetrical cells and single cells

Electrode powders were homogeneously mixed with a 6 wt% ethyl cellulose–terpineol binder to form electrode slurries. The slurries were symmetrically screen-printed on both sides of GDC and calcined at 950 °C for 2 h to prepare symmetric cells. The cathode paste was printed onto commercial half-cells (Ni–YSZ|YSZ|GDC, Ningbo Sofman Energy Co., Ltd., China) and calcined at 950 °C for 2 h. The fuel cell was then attached to a quartz tube, with the anode side sealed using conductive adhesive (DAD-87) to obtain a single cell for *I*–*V* and stability measurements.

2.3 Structural characterization and electrical performance testing

The phase structure of the material was characterized by X-ray diffraction (XRD; D/Max-2000/PC, Rigaku, Japan) with a Cu Kα radiation source (λ = 0.154,05 nm) operated at 40 kV and 200 mA. The phase structure and elemental distribution of the cathode material were characterized by a field-emission scanning electron microscope (FE-SEM; 7610, JEOL, Japan), and the average grain size was analyzed using ImageJ software. The spatial arrangement of the crystals was observed using a high-resolution transmission electron microscope (HRTEM; JEM-2100-F, JEOL, Japan) equipped with elemental mapping and energy-dispersive X-ray spectroscopy (EDX). The specific surface area was measured via N_2 adsorption–desorption isotherm experiments (ASAP 2010, Micromeritics, USA) under vacuum conditions after degassing the sample at 150 °C for 10 h. Thermogravimetric analysis (TGA) data were collected using a thermogravimetric analyzer under a nitrogen atmosphere, with a temperature range of RT-800 °C. The thermal expansion coefficient (TEC) of the materials was measured using a thermal dilatometer (Dil402C, Netzsch, Germany). The chemical environment and valence state distribution characteristics of each element in the materials were investigated via X-ray photoelectron spectroscopy (XPS; ESCALAB 250, VG, UK). The O_2 temperature-programmed desorption was tested using a hydrogen storage high-pressure adsorption instrument (H-Sorb 2600PCT). The oxygen vacancies in the materials were measured using an electron paramagnetic resonance (EPR) spectrometer (A300, Bruker, Germany). Electrochemical impedance spectroscopy (EIS) data of the batteries were collected using an electrochemical workstation (1260/1287, Transfusion Power, UK), with a test frequency range of 10^{-1}–10^{-5} Hz and a disturbance signal amplitude of 30 mV. EIS tests for both oxygen partial pressure (p_{O_2}) and CO_2 tolerance were carried out in a sealed tube furnace. The chemical oxygen diffusion coefficient (D_{chem}) and surface exchange coefficient (K_{ex}) of the electrodes were quantified using the electrical conductivity relaxation (ECR) technique [6]. Fourier transform infrared spectroscopy (FT-IR) was used to detect the functional groups of the CO_2 heat-treated materials. During polarization curve testing, air (99.999% purity, flow rate: 100 mL·min^{-1}) was introduced in SOFC mode, while humidified air (containing 3% H_2O) was used in SOEC mode. All symmetric cell tests are carried out under flowing air, and for single-cell tests, H_2 (with 3% H_2O, flow rate: 100 mL·min^{-1}) is supplied to the anode side, while air (99.999% purity, flow rate: 100 mL·min^{-1}) is fed to the cathode side.

2.4 Density functional theory calculation

All DFT calculations were performed using the Vienna *Ab initio* Simulation Package (VASP). By referring to the Monte Carlo tree search with graph theory-based distance matrix (MCTSGT) method, the initial DFT configurations of $La_{11}Sr_7Co_4Fe_{14}O_{54}$, $La_4Sr_4Pr_4Nd_3Ba_3Co_4Fe_{14}O_{54}$ (with the *Pm3m* structure), and $La_4Sr_3Pr_3Nd_3Ba_3Co_3Fe_{13}O_{48}$ (with the *Pbnm* structure) can be obtained [22]. First, crystallographic sites of ABO_3 perovskites were grouped by chemical environment, and supercells were expanded to achieve integer atomic occupancies, avoiding fractional occupation. Next, based on configurational entropy, $La_{11}Sr_7Co_4Fe_{14}O_{54}$ used coulomb energy as the objective function, while the two high-entropy models adopted Warren–Cowley short-range order parameters to ensure random cation distribution. Monte Carlo tree search (MCTS) with an upper confidence bound applied to trees (UCT) strategy explored the configuration space, balancing exploration and exploitation. Graph theory-based distance matrices pruned symmetrically equivalent nodes to reduce redundancy. Finally, DFT relaxation (PBE-GGA, PAW) was performed while preserving *Pm3m* cubic or *Pbnm* orthorhombic symmetry, matching experimental lattice parameters for reliable computational models. Exchange-correlation effects were modeled via the Perdew–Burke–Ernzerhof (PBE) functional (within the generalized gradient approximation, GGA), and core-valence interactions were treated with the projected augmented wave (PAW) method. A 400 eV plane-wave energy cutoff and 2 × 2 × 1 Monkhorst-Pack *k*-point grid were used for Brillouin zone sampling. Structural optimization converged to 1.0×10^{-5} eV (energy) and 0.05 eV·Å^{-1} (force), with van der Waals (vdW) interactions accounted for by the DFT-D3 method. The adsorption energy (E_{ads}) is defined as Eq. (1):

$$E_{ads} = E_{complex} - E_{substrate} - E_{adsorbate} \tag{1}$$

where $E_{substrate}$ and $E_{adsorbate}$ are the energies of the substrate surface and adsorbate molecule, respectively.

3 Results and discussion

3.1 Morphological and structural analysis

Typically, a perovskite oxide is classified as an HEP when its configurational entropy (S_{config}) exceeds $1.5R$. S_{config} can be calculated using Eq. (2) [23]:

$$S_{config} = -R\left[\left(\sum_{a=1}^{A} X_a \ln X_a\right)_{\text{A-site}} + \left(\sum_{b=1}^{B} X_b \ln X_b\right)_{\text{B-site}} + \left(\sum_{c=1}^{C} X_c \ln X_c\right)_{\text{O-site}}\right] \tag{2}$$

where R is the universal gas constant; A, B, and C are the number of distinct elements at the perovskite's A-site, B-site, and O-site, respectively; and X_a, X_b, and X_c are the mole fractions of the elements at these sites, respectively. The configurational entropy of HELSCF is approximately $2.11R$, which exceeds $1.5R$, so it belongs to a HEP. To gain an in-depth understanding of the crystal structure of the electrode materials, Fig. 1(a) presents the XRD patterns of LSCF and high-entropy HELSCF calcined at 1000 and 1100 °C, respectively. According to locally amplified regions 1 and 2, obvious structural differences exist between HELSCF-*Pbnm*, LSCF-*Pm3m*, and HELSCF-*Pm3m*. LSCF calcined at 1000 °C and HELSCF sintered at 1100 °C both exhibit a cubic perovskite structure. In contrast, HELSCF prepared at 1000 °C adopts an orthorhombic perovskite configuration. For convenience of discussion, LSCF is denoted as LSCF-*Pm3m*, while HELSCF with cubic and orthorhombic structures are designated as HELSCF-*Pm3m* and HELSCF-*Pbnm*, respectively. To further verify the crystal structures of the electrode materials, Fig. S1 in the Electronic Supplementary Material (ESM), Figs. 1(b) and 1(c) present the Rietveld-refined XRD patterns of LSCF-*Pm3m*, HELSCF-*Pm3m*, and HELSCF-*Pbnm*, respectively, and Table S1 in the ESM lists the corresponding refinement parameters. It can be observed that LSCF forms a cubic phase with the *Pm3m* space group when calcined at 1000 °C, whereas HELSCF exhibits an asymmetric orthorhombic perovskite structure. Only when the calcination temperature is increased to 1100 °C can HELSCF form a cubic phase. This phenomenon may be attributed to the presence of more cations at the A-site of high-entropy oxides, which are more prone to distortion. Thus, an elevated calcination temperature is required to enhance the symmetry during crystal formation. It is evident that the crystal structure of HELSCF can be regulated by controlling the calcination temperature. In addition, Figs. 1(d)–1(f) display SEM images of LSCF-*Pm3m*, HELSCF-*Pm3m*, and HELSCF-*Pbnm*, respectively, while Fig. S2 in the ESM presents the corresponding grain size distribution diagrams obtained using ImageJ software. The results indicate that

https://doi.org/10.26599/JAC.2026.9221315

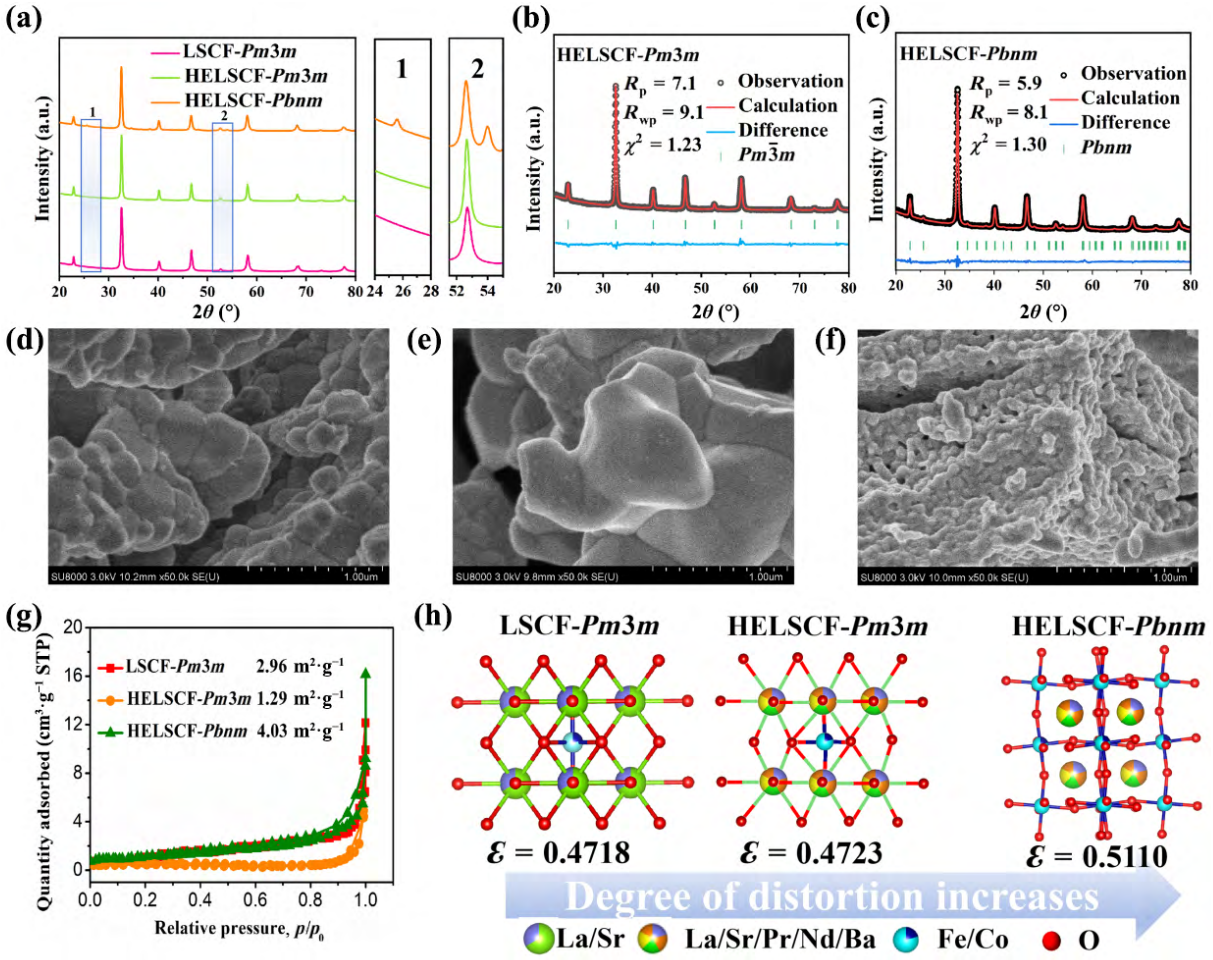

Fig. 1 (a) XRD patterns of all electrodes and Rietveld-refined XRD patterns of (b) HELSCF-*Pm*3*m* and (c) HELSCF-*Pbnm*; SEM images of (d) LSCF-*Pm*3*m*, (e) HELSCF-*Pm*3*m*, and (f) HELSCF-*Pbnm*; (g) nitrogen adsorption–desorption isotherms of all electrodes and (h) corresponding schematic diagrams of lattice distortion degrees.

HELSCF-*Pbnm* exhibits a smaller grain size, whereas HELSCF-*Pm*3*m* undergoes the most severe grain coarsening due to the excessively high calcination temperature, which is consistent with the Ostwald ripening phenomenon [21]. Typically, smaller grains contribute to an increased specific surface area [24]. Therefore, Fig. 1(g) displays the specific surface areas of all electrodes, revealing that HELSCF-*Pbnm* (4.03 m²·g⁻¹) has a higher specific surface area than LSCF-*Pm*3*m* (2.96 m²·g⁻¹) and HELSCF-*Pm*3*m* (1.29 m²·g⁻¹), which is consistent with the observed SEM results. A higher specific surface area facilitates an increase in the active sites for the cathode material to contact oxygen, thereby promoting ORR kinetics [25].

As is well established, the high-entropy effect induces lattice distortion and reduces structural symmetry. To evaluate the distortion degree (ε) in different crystal structures, the ε of the electrodes can be calculated using Eq. (3) [14]:

$$\varepsilon=\left(\frac{1}{3}\right)\left[\left(\frac{a_{\text{norm}}-a_{\text{ps.cubic}}}{a_{\text{ps.cubic}}}\right)^2+\left(\frac{b_{\text{norm}}-b_{\text{ps.cubic}}}{b_{\text{ps.cubic}}}\right)^2+\left(\frac{c_{\text{norm}}-c_{\text{ps.cubic}}}{c_{\text{ps.cubic}}}\right)^2\right]^{\frac{1}{2}} \tag{3}$$

where $a_{\text{ps.cubic}}$ is the pseudocubic lattice parameter, and a_{norm}, b_{norm}, and c_{norm} are the normalized pseudocubic lattice parameters of the lower-symmetry unit cell, respectively. These parameters can be calculated using Eqs. (4) and (5):

$$a_{\text{ps.cubic}}=\sqrt[3]{V} \tag{4}$$

$$a_{\text{norm}}=\frac{a}{\sqrt[3]{V}\sqrt{2}},\ b_{\text{norm}}=\frac{b}{\sqrt[3]{V}\sqrt{2}},\ c_{\text{norm}}=\frac{c}{\sqrt[3]{V}\sqrt{2}} \tag{5}$$

where a, b, c, and V are the actual unit cell parameters of the electrodes, which can be referenced from the XRD refinement parameters in Table S1 in the ESM. Figure 1(h) presents schematic diagrams of the lattice distortion and the calculated ε for LSCF-*Pm*3*m*, HELSCF-*Pm*3*m*, and HELSCF-*Pbnm*. It can be observed that in the same cubic structure, the ε value of HELSCF-*Pm*3*m* is higher than that of LSCF-*Pm*3*m* due to the lattice distortion induced by high entropy. Additionally, HELSCF-*Pbnm* itself has an orthorhombic structure with unequal bond lengths in different directions, which leads to more lattice distortion. Thus, the ε value is further increased compared to that of HELSCF-*Pm*3*m*.

To investigate the effect of lattice distortion on the internal crystal lattice, Figs. 2(a)–2(c) present scanning transmission electron microscopy (STEM) images, HRTEM images, and selected area electron diffraction (SAED) patterns of LSCF-*Pm*3*m*, respectively. In Fig. 2(b), the lattice spacing of 0.392 nm corresponds to the (100) crystal plane of the *Pm*3*m* space group. Moreover, the HRTEM and SAED images indicate that the cubic perovskite structure exhibits excellent symmetry. Figures 2(d)–2(f) present the STEM, HRTEM, and SAED images of HELSCF-

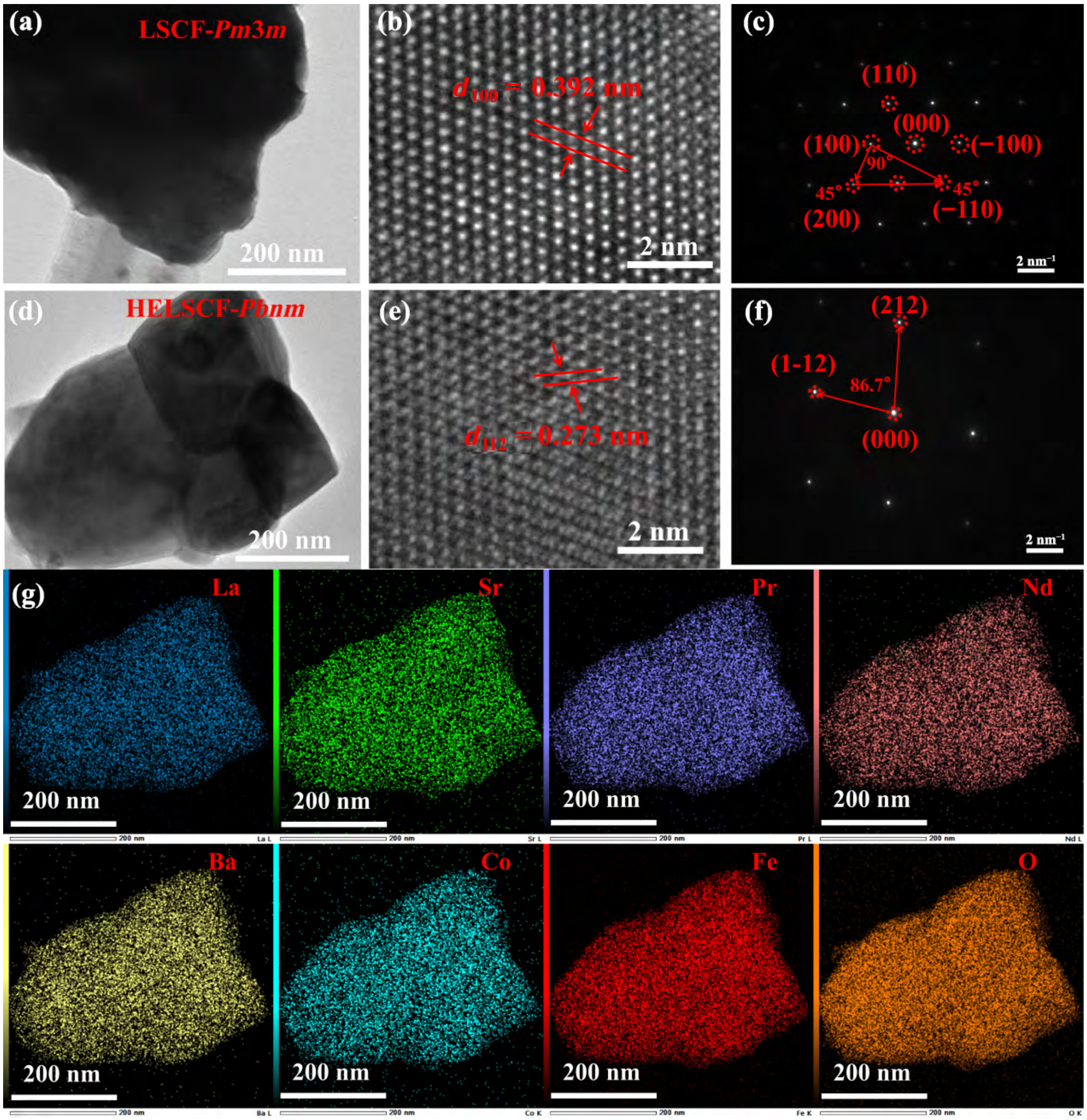

Fig. 2 (a) STEM image, (b) HRTEM image, and (c) SAED pattern of LSCF-*Pm*3*m*; (d) STEM image, (e) HRTEM image, (f) SAED pattern, and (g) EDS elemental mapping of HELSCF-*Pbnm*.

Pbnm, respectively. In Fig. 2(e), the lattice spacing of 0.273 nm corresponds to the (112) crystal plane of HELSCF-*Pbnm*. In contrast to the symmetric arrangement of LSCF-*Pm*3*m*, a large number of lattice distortion phenomena are observed in HELSCF-*Pbnm*, which stems from the A-site high-entropy effect and asymmetric orthorhombic perovskite characteristics. Figure 2(g) displays the EDS elemental mapping of HELSCF-*Pbnm*, where all elements are uniformly distributed without any aggregation. This indicates that no other phases precipitated in HELSCF-*Pbnm*. All the aforementioned results confirm that the high-entropy effect and the unique orthorhombic phase structure are conducive to enhancing lattice distortion in the perovskite structure.

3.2 Electrocatalytic activity and electrochemical cell performance analysis

Oxygen vacancies are one of the crucial factors for evaluating the catalytic activity of cathodes. To better analyze the effect of the high-entropy effect on oxygen vacancies in the material, the O 1s XPS spectrum can distinguish the surface chemical environment of O in different materials. In Fig. 3(a), the O 1s peaks of the three electrodes (LSCF-*Pm*3*m*, HELSCF-*Pm*3*m*, and HELSCF-*Pbnm*) are all fitted into three Gaussian components, corresponding to three oxygen states in the material: the lattice oxygen (O_{lattice}, ~527.7 eV) has the lowest binding energy; the surface active oxygen (O_{surface}, ~530.1 eV), whose binding energy is slightly lower than that of lattice oxygen, serves as the key active site for electrocatalytic reactions [26]; and the oxygen with the highest binding energy is related to the physically adsorbed water molecules on the electrode surface (H_2O_{surface}, ~532.1 eV) [27]. The O 1s results show that the O_{surface} proportion of HELSCF-*Pbnm* (52.70%) is higher than that of HELSCF-*Pm*3*m* (51.93%) and LSCF-*Pm*3*m* (50.06%), indicating that the high-entropy orthorhombic phase structure is more prone to releasing O_{lattice} to form surface active oxygen sites. The EPR spectrum can directly determine the variation trend of defects in the crystal by detecting the number of unpaired electrons in the system [28]. In Fig. 3(b), the characteristic signal at g = 2.002 corresponds to the unpaired electrons in the O 2p orbital induced by oxygen vacancies [29,30]. When oxygen vacancies form, the 2p orbital electrons of the surrounding O atoms become delocalized, and the signal intensity is proportional to the oxygen vacancy content. The EPR results indicate that the oxygen vacancy concentration of HELSCF-*Pm*3*m* is higher than that of LSCF-*Pm*3*m*, confirming that the distortion induced by the high-entropy effect facilitates the formation of oxygen vacancies. Furthermore, among HEPs with the same composition, HELSCF-*Pbnm* exhibits a stronger EPR signal intensity than HELSCF-*Pm*3*m*, which can be attributed to the regulation of structural symmetry contributing to the further optimization of the oxygen vacancy content in HEPs.

Typically, the formation of perovskite oxides is often accompanied by the reduction of B-site ions [31]. Figure 3(c) and Fig. S3 in the ESM present the XPS spectra of the Fe 2p and Co 2p orbitals for all electrodes, respectively. Table 1 shows the contents of Fe and Co ions with different valence states as well as their average valence states in all electrodes. Both Fe and Co ions exhibit mixed valence states, and with the increase in oxygen vacancy content, the average valence state of B-site ions decreases accordingly, which is consistent with the variation trend of oxygen vacancy content [3].

To systematically evaluate the effect of the high-entropy effect on the electrocatalysis-related properties of the electrodes, Fig. 3(d) presents the electrical conductivity curves of all electrodes as a function of temperature. The data indicate that below approximately 400 °C, the electrical conductivity of all electrodes increases due to thermal activation, which enhances the hopping conduction of small polarons [32]. However, when the temperature exceeds 400 °C, a large amount of lattice oxygen in the electrodes is released to form oxygen vacancies, which hinder the charge transport path and thus lead to a decrease in electrical conductivity [33]. A similar phenomenon can also be observed

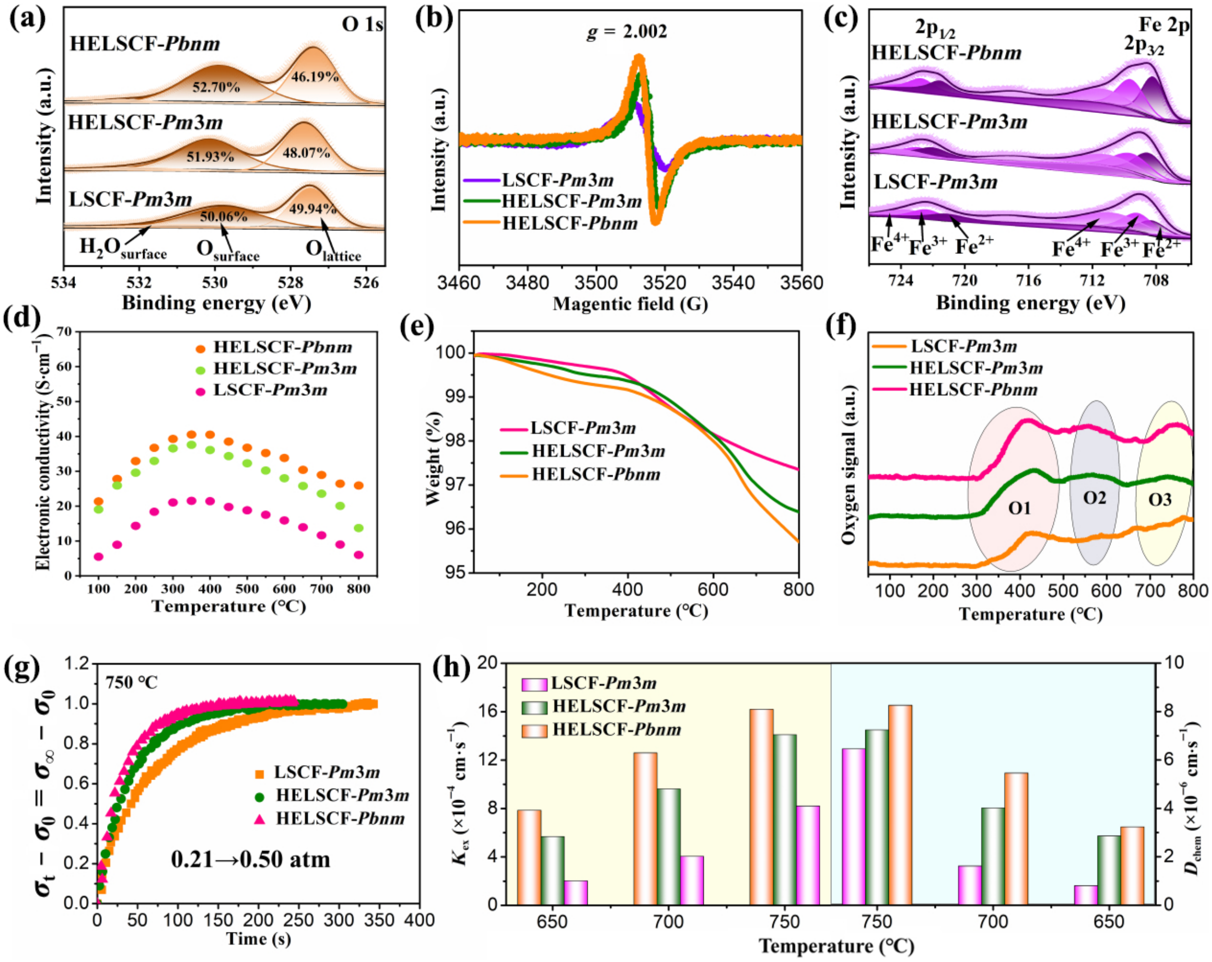

Fig. 3 (a) XPS spectra of the O 1s orbital, (b) EPR curves, and (c) XPS spectra of the Fe 2p orbitals for all electrodes. (d) Electrical conductivity curves of all electrodes in the temperature range of 100–800 °C, (e) Tg curves, and (f) O_2-TPD curves in the range of 30–800 °C. (g) ECR curves of all electrodes at 750 °C, and (h) K_{ex} and D_{chem} values in the temperature range of 650–750 °C.

Table 1 Proportion and average valence state of Co and Fe ions with different valence states among all electrodes

Electrode	Co			Fe			
	Co^{2+} (%)	Co^{3+} (%)	Average valence	Fe^{2+} (%)	Fe^{3+} (%)	Fe^{4+} (%)	Average valence
LSCF-*Pm*3*m*	45.73	54.27	2.54	22.24	31.52	46.24	3.24
HELSCF-*Pm*3*m*	58.58	41.42	2.41	30.55	31.26	38.09	3.07
HELSCF-*Pbnm*	62.93	37.07	2.37	31.61	32.53	35.86	3.04

from the thermogravimetric (TG) curves in Fig. 3(e): the weight loss of the electrodes intensifies above 400 °C, which is mainly associated with the release of lattice oxygen. Moreover, HELSCF-*Pbnm* exhibits the highest weight loss ratio, suggesting that it forms the largest number of oxygen vacancies. Conductivity test results reveal that A-site high-entropy engineering contributes to enhancing the perovskite conductivity. This is attributed to the optimization of the perovskite's electronic structure by high-valent Pr^{3+}/Pr^{4+} and Nd^{3+} ions in the crystal, which provides more charge carriers available for transport in the electrode.

The oxygen temperature-programmed desorption (O_2-TPD) technique facilitates the analysis of oxygen vacancy formation and the ORR activity of electrodes during operation. Three characteristic oxygen peaks are observed in the O_2-TPD curves of Fig. 3(f). The O1 peak (300–500 °C) originates from adsorbed/desorbed oxygen on the cathode surface and oxygen vacancies [34]; a larger integrated area indicates a higher bulk oxygen vacancy content. The O2 peak (500–700 °C) is associated with the reduction of high-valence B-site ions to intermediate-valence states (forming oxygen vacancies), which promotes lattice oxygen migration from the cathode interior to the surface [35]. The O_3 peak above 700 °C arises from further reduction of intermediate-valence B-site ions, leading to additional oxygen vacancy formation [36]. From the O_2-TPD results, it can be seen that the HELSCF has higher contents of both its inherent oxygen vacancies and the additional oxygen vacancies released under high-temperature conditions compared with the pristine LSCF, theoretically exhibiting better electrocatalytic activity.

The oxygen exchange coefficient (K_{ex}) and chemical bulk diffusion coefficient (D_{chem}) are key parameters for surface oxygen exchange and oxygen ion diffusion kinetics[37–39]. When the p_{O_2} changes abruptly, the formation and annihilation of oxygen vacancies are accompanied by the migration of electrons or holes to maintain charge balance [3]. Therefore, the redistribution of oxygen is achieved through the synergistic effect of surface hole migration and bulk charge compensation processes, which is known as the ECR phenomenon [40]. This implies that the adsorption and diffusion process of surface oxygen is closely related to the surface oxygen vacancy concentration [41], while bulk diffusion is proportional to the degree of structural defects [42,43]. This mechanism can be described using Reactions (6)–(8) [44]:

$$O_2(g) \rightarrow O_{2,\mathrm{ads}} \tag{6}$$

$$2V_{O(\mathrm{surface})}^{\cdot\cdot} + O_{2,\mathrm{ads}} \rightarrow 2V_{O(\mathrm{surface})}^{\times} + 4h^{\cdot} \tag{7}$$

$$V_{O(\mathrm{surface})}^{\times} + V_{O(\mathrm{bulk})}^{\cdot\cdot} \rightarrow V_{O(\mathrm{surface})}^{\cdot\cdot} + O_{O(\mathrm{bulk})}^{\times} \tag{8}$$

where $V_O^{\cdot\cdot}$, $O_O^{\times}$, and $h^{\cdot}$ are the oxygen vacancies, lattice oxygen, and electron holes, respectively. Figure 3(g) shows the ECR curves of all electrodes at 750 °C when the p_{O_2} is switched from 0.21 to 0.50 atm. By calculating and fitting the ECR curves, the K_{ex} and D_{chem} values of the samples can be obtained, with the relevant calculation formulas provided in the supporting information. The data indicate that the ORR kinetics of HELSCF-*Pm*3*m* outperform those of LSCF-*Pm*3*m* because the distortion induced by the high-entropy structure generates a higher concentration of oxygen vacancies, which promotes the adsorption of surface oxygen ions on the electrode surface and the transport rate of dissociated oxygen ions at these vacancies. In contrast, compared to HELSCF-*Pm*3*m*, HELSCF-*Pbnm* further accelerates ORR kinetics, as its asymmetric crystal structure facilitates additional distortion. The ECR curves of all electrodes are presented in Fig. S4 in the ESM. Figure 3(h) displays the K_{ex} and D_{chem} values of all electrodes over the temperature range of 650–750 °C. The results show that at the same temperature, HELSCF-*Pbnm* exhibits the fastest kinetics for both surface oxygen exchange and oxygen ion diffusion. The Arrhenius plots of K_{ex} and D_{chem} for all electrodes are shown in Fig. S5 in the ESM. These results further confirm that HELSCF can significantly reduce the energy barrier required for ORR kinetic reactions.

Figure 4(a) shows the EIS curves of symmetric cells fabricated with all electrodes at 750 and 700 °C. For ease of comparison, the ohmic resistance (arising from the current-collecting assembly and electrolyte thickness) was subtracted from all EIS data and is presented in Table S2 in the ESM. According to the area-specific resistance (ASR) values, high-entropy LSCF exhibits lower ASR. Specifically, the ASR of HELSCF-*Pbnm* is 0.040 $\Omega\cdot cm^2$ at 750 °C, which is lower than that of HELSCF-*Pm*3*m* (0.084 $\Omega\cdot cm^2$) and LSCF-*Pm*3*m* (0.123 $\Omega\cdot cm^2$). Figure 4(b) presents the distribution of relaxation times (DRTs) corresponding to the EIS curves of LSCF-*Pm*3*m*, HELSCF-*Pm*3*m*, and HELSCF-*Pbnm* at 750 °C. Three characteristic peaks are observed in the DRT curves, representing different electrochemical reaction processes of the electrode materials: high-frequency (HF) corresponds to charge transfer [45], intermediate-frequency (IF) corresponds to oxygen adsorption/dissociation, and low-frequency (LF) corresponds to gas diffusion on the electrode surface [4,46]. Based on DRT analysis, compared with LSCF-*Pm*3*m*, HELSCF-*Pm*3*m* exhibits faster oxygen adsorption and dissociation rates, while HELSCF-*Pbnm* can comprehensively enhance the electrocatalytic activity of the electrode material. This can be attributed to the local disorder induced by the high-entropy effect combined with the synergistic effect of the asymmetric crystal structure, which promotes the oxygen adsorption/dissociation and charge transport processes. Figure S6 in the ESM shows the corresponding simplified mechanism diagram. Figure S7 in the ESM presents the EIS curves of these three types of electrodes over the temperature range of 600–750 °C, and Fig. 5(c) displays the corresponding activation energies (E_a). The formula for calculating E_a is as shown in Eq. (9):

$$\mathrm{ASR} = \frac{T}{A}\exp\left(\frac{-E_a}{kT}\right) \tag{9}$$

where T, A, and k are the absolute temperature, preexponential factor, and Boltzmann constant (8.62×10^{-5} eV·K^{-1}), respectively.

It can be observed that HELSCF-*Pbnm* exhibits the lowest reaction energy barrier, which facilitates the occurrence of the ORR on the electrode. The HELSCF-*Pbnm* mentioned in this work is expected to be a highly promising cathode material for SOFCs. Figure 4(d) presents the polarization curves of the three electrodes under SOFC and SOEC modes at 750 °C, which evaluate the bifunctional electrocatalytic performance of the electrode materials. The performance of the HELSCF-*Pbnm* electrode outperforms that of the other electrodes in both modes: at an overpotential of η = 100 mV, the current densities of the HELSCF-*Pbnm* electrode reach approximately 216.3 A·cm^{-2} (for SOFC) and 212.6 mA·cm^{-2} (for SOEC). The exchange current density (i_0) is an effective parameter for assessing electrocatalytic activity. At high current densities, its relationship with the overpotential η can be described by the Tafel (Eq. (10)) [47,48]:

$$\eta = \left(\ln(i_0) + \frac{RT}{nF\beta}\right) \times \ln i \tag{10}$$

where β is the charge transfer coefficient for the cathodic and anodic reactions. Figure 4(e) shows the Tafel plots of the three

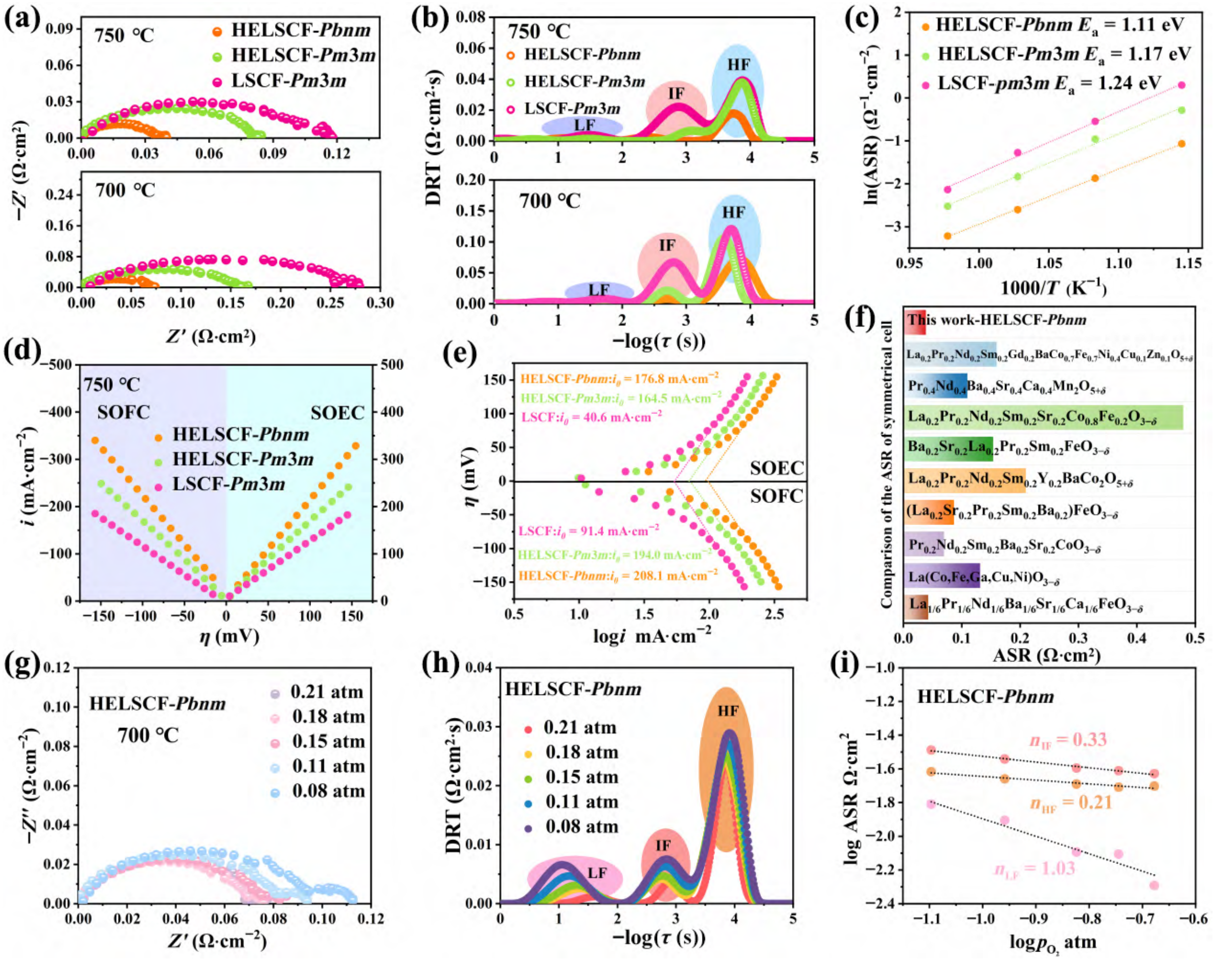

Fig. 4 (a) EIS curves, (b) corresponding DRT curves of all electrodes at 700 and 750 °C, and (c) Arrhenius plots of all electrodes; (d) polarization curves and (e) corresponding Tafel plots of all electrodes under SOFC and SOEC modes at 750 °C. (f) Comparison plot of the ASR between HELSCF-*Pbnm* and previously reported ABO_3 HEP electrodes at 750 °C. (g) EIS curves, (h) corresponding DRT curves, and (i) p_{O_2}-dependent linear relationship plots of the HELSCF-*Pbnm* electrode at 700 °C.

electrodes at 750 °C. The HELSCF-*Pbnm* electrode exhibits the largest i_0 values in both the ORR and OER modes (208.1 and 176.8 mA·cm^{-2}), which are significantly higher than those of HELSCF-*Pm3m* (194.8 and 164.5 mA·cm^{-2}) and LSCF-*Pm3m* (91.4 and 40.6 mA·cm^{-2}). Figures S8 and S9 in the ESM show the polarization curves and Tafel plots of all electrodes in the temperature range of 600–700 °C. HELSCF-*Pbnm* exhibits the highest electrocatalytic activity among all samples, and its current density in SOFC mode is higher than that in SOEC mode, indicating that HELSCF-*Pbnm* is more suitable as a cathode for SOCs. Figure 4(f) compares the ASR values of HELSCF-*Pbnm* with those of other ABO_3-type HEPs at 750 °C [49–57]. Integrating the electrocatalytic activity test results, HELSCF-*Pbnm* functions as an excellent bifunctional electrode.

Testing the EIS curves of electrodes under different p_{O_2} helps understand the rate-limiting step (RLS) of the ORR kinetics for cathode materials. Among the results, Fig. 4(g) and Fig. S10 in the ESM present the EIS curves of HELSCF-*Pbnm*, LSCF-*Pm3m*, and HELSCF-*Pm3m* at 700 °C under varying p_{O_2}. The ASR values of all electrodes increase with decreasing p_{O_2}, which is consistent with the characteristics of oxygen electrodes. Figure 4(h) and Fig. S11 in the ESM show the DRT curves corresponding to the EIS data of HELSCF-*Pbnm*, LSCF-*Pm3m*, and HELSCF-*Pm3m* under different p_{O_2} values. Figure 4(i) and Fig. S12 in the ESM present the RLS corresponding to the impedance at various frequencies. The dependence of impedance on p_{O_2} can be analyzed using Eq. (11) [58]:

$$\mathrm{ASR}=k(p_{O_2})^{-n} \tag{11}$$

where k is the independent coefficient. The RLS of each ASR can be determined by the value of n (Reactions (12)–(15)) [59]:

$$n = 1, \mathrm{O_2} \Leftrightarrow \mathrm{O_{2,ads}} \tag{12}$$

$$n = 0.5, \mathrm{O_{2,ads}} \Leftrightarrow 2\mathrm{O_{ads}} \tag{13}$$

$$n = 0.25, 2\mathrm{O_{ads}} + 2e^- + \mathrm{V_O^{\cdot\cdot}} = \mathrm{O_O^{\times}} \tag{14}$$

$$n = 0, \mathrm{O^{2-}_{electrode}} \Leftrightarrow \mathrm{O^{2-}_{electrolyte}} \tag{15}$$

Analysis indicates that the RLS of HELSCF-*Pbnm* at HF are primarily charge transfer and oxygen ion transport across the triple-phase boundary to the electrolyte. At IF, the RLS mainly involves oxygen adsorption/dissociation and charge transfer processes, while the LF region is closely associated with the gas diffusion rate on the electrode surface. A comparison of the RLS at different frequencies reveals that HELSCF-*Pbnm* exhibits a stronger dependence of oxygen adsorption and dissociation rates on variations in p_{O_2}. This phenomenon can be attributed to the higher oxygen vacancy content of HELSCF-*Pbnm* [29].

Evaluating the electrocatalytic activity of electrodes through single-cell fabrication is crucial. Figure 5(a) presents the cross-sectional SEM image of the single cell, where HELSCF-*Pbnm* is

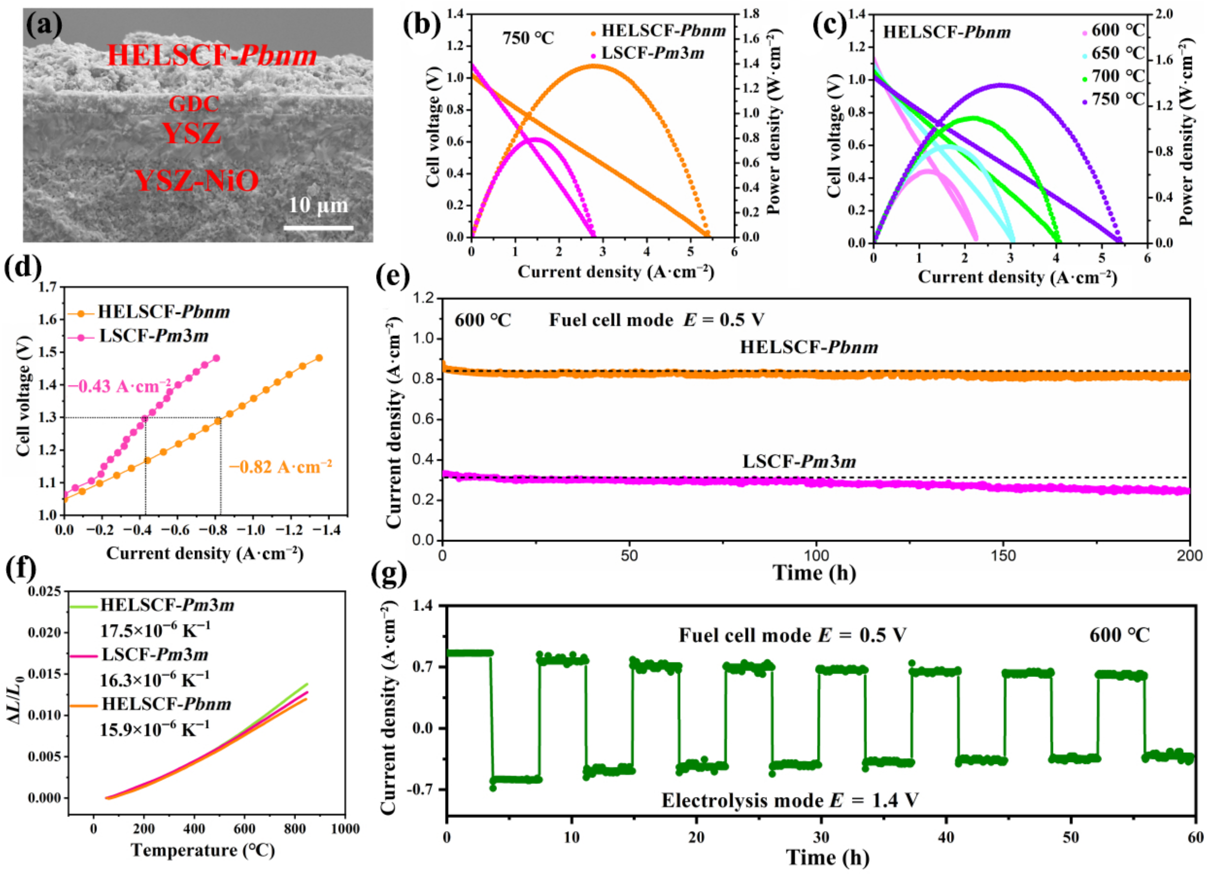

Fig. 5 (a) Cross-sectional view of the single cell, (b) *I–V–P* curves of HELSCF-*Pbnm* and LSCF-*Pm3m* single cells in FC mode at 750 °C, (c) *I–V–P* curves of HELSCF-*Pbnm* in FC mode over the temperature range of 600–750 °C, (d) *I–V* curves of HELSCF-*Pbnm* and HELSCF-*Pm3m* single cells in EC mode at 750 °C, (e) long-term stability of the LSCF-*Pm3m* and HELSCF-*Pbnm* single cells in FC mode at 600 °C, and (f) TEC curves of all electrodes in the temperature range of 50–850 °C. (g) Reversible cycling stability curve of the HELSCF-*Pbnm* single cell.

employed as the primary oxygen electrode (~15 μm). GDC acts as a buffer layer (~4 μm) between the oxygen electrode and the Y_2O_3-stabilized ZrO_2 (YSZ) electrolyte (~8 μm) to inhibit the reaction of Ba^{2+} and Sr^{2+} ions with Zr^{4+} ions to form zirconates, which would deteriorate cell stability. NiO–YSZ is used as the hydrogen electrode (~380 μm). Figures 5(b) and 5(d) compare the *I–V–P* curves (fuel cell, FC mode) and *I–V* curves (electrolysis cell, EC mode) of the HELSCF-*Pbnm*-based cell and the LSCF-*Pm3m*-based cell at 750 °C. As seen from the *I–V* curves, the open-circuit voltages (OCVs) of the single cells do not reach the theoretical OCV (~1.1 V) calculated by the Nernst equation. This can be attributed to the insufficient sealing performance of the conductive adhesive during single-cell packaging. However, at 750 °C, the OCVs of the LSCF-*Pm3m*-based single cell and the HELSCF-*Pbnm*-based single cell are 1.03 and 1.08 V, respectively. The maximum power density (MPD) of the HELSCF-*Pbnm*-based single cell is 1.38 W·cm^{-2}, which is 1.7 times that of the LSCF-*Pm3m*-based single cell (0.81 W·cm^{-2}). Therefore, although there is a slight difference in OCV, it does not affect the conclusion regarding the performance comparison of MPD. At a voltage of 1.3 V, the current density of the HELSCF-*Pbnm*-based cell is 0.82 A·cm^{-2}, significantly outperforming the LSCF-*Pm3m*-based cell (0.43 A·cm^{-2}). The electrocatalytic performance of HELSCF-*Pbnm* under EC operation still lags significantly behind existing reports [45,56,60]. Therefore, HELSCF-*Pbnm* is more suitable for operation in FC mode. In future research, efforts can be devoted to enhancing the electrocatalytic performance under the EC mode in similar systems. Figure S13 in the ESM presents the EIS curves of the two single cells at OCV within the temperature range of 600–750 °C. At the same temperature, the *ASR* values of the HELSCF-*Pbnm* single cell are all lower than those of LSCF-*Pm3m*. Furthermore, Fig. 5(c) and Fig. S14 in the ESM present the MPD of the HELSCF-*Pbnm*-based single cell and LSCF-*Pm3m*-based single cell at temperatures ranging from 750 to 600 °C, with MPD values of 1.38, 1.15, 0.84, and 0.59 W·cm^{-2}, respectively. A comparison with Table S3 in the ESM confirms that the HELSCF-*Pbnm*-based single cell possesses significant electrochemical performance advantages. Considering that HELSCF-*Pbnm*-based single cells exhibit better electrochemical performance in both SOFCs and SOECs, the enhanced electrocatalytic performance cannot be simply attributed to the increase in oxygen vacancy concentration. Instead, the more intrinsic driving force may lie in the high-entropy-induced lattice distortion and electronic structure reconstruction, which jointly enhance the activation capability and accelerate the surface exchange/bulk diffusion kinetics. In contrast, the variation in oxygen vacancies is only one of the characteristics reflecting this structure-electron coupling effect. We will further discuss the effects of high-entropy-induced distortion and electronic reconstruction on electrocatalytic activity in subsequent sections. In addition, long-term stability is also a crucial parameter for evaluating single-cell electrodes. Figure 5(e) shows the long-term stability of the LSCF-*Pm3m* and HELSCF-*Pbnm* single cells at 600 °C under a constant voltage of 0.5 V over 200 h. During the test, almost no obvious degradation in current density was observed for HELSCF-*Pbnm*, whereas LSCF-*Pm3m* displayed a pronounced downward trend. The TEC mismatch between different components is a critical factor governing the long-term stability of cells [61]. To rationalize this observation, Fig. 5(f) displays the TEC values of all electrodes. In comparison with LSCF-*Pm*3*m*, HELSCF-*Pbnm* possesses a significantly reduced TEC and improved thermal compatibility with the GDC (12.5×10^{-6} K^{-1}) component [62], which consequently contributes to the enhanced long-term stability of the cell. Furthermore, Fig. S15 in the ESM and Fig. 5(g) evaluate the stability of the LSCF-*Pm*3*m* and HELSCF-*Pbnm* cells under repeated switching between fuel cell (FC) and electrolysis cell (EC) modes, respectively. Both HELSCF-*Pbnm* and LSCF-*Pm*3*m* exhibit degradation during cycling, yet the degradation of LSCF-*Pm*3*m* is significantly more pronounced. Figure S16 in the ESM presents the EIS profiles of the two cells at different stages during the long-term stability test, further confirming that HELSCF-*Pbnm* possesses superior overall stability. The degradation observed in the cycling stability test can be attributed to two main factors. First, slight degradation occurs after the 200 h long-term test due to the mismatch in TEC among components. Second, under EC mode, part of the H_2O deposited on the surface is not electrolyzed in a timely manner, and alkaline-earth metal ions are more easily induced by H_2O molecules [21], leading to partial decomposition of the electrode. In addition, the higher surface acidity of HELSCF-*Pbnm* effectively suppresses the reaction between alkaline-earth metal ions and H_2O. In contrast, the weaker H_2O electrolysis capability of LSCF-*Pm*3*m* results in more H_2O molecules accumulating on the surface, thus causing more severe degradation. Similarly, highly acidic ions also help improve the CO_2 tolerance of the material, which will be analyzed in subsequent sections. To verify this mechanism, Fig. S17 in the ESM shows the XRD patterns of the LSCF-*Pm*3*m* and HELSCF-*Pbnm* samples calcined in a 3% H_2O atmosphere for 40 h. HELSCF-*Pbnm* exhibits a much more stable phase structure, whereas LSCF-*Pm*3*m* undergoes substantial structural decomposition with the formation of numerous impurity phases.

3.3 Density functional theory analysis

To elucidate the intrinsic correlation between the high-entropy effect and ORR activity at the atomic level, DFT calculations were conducted on all electrodes to analyze the electronic structures of electrodes [63]. It is well established that oxygen adsorption and dissociation on the electrode surface determine ORR activity, and previous studies have confirmed that the most favorable oxygen adsorption sites are B-site atoms on the BO_2-terminated perovskite surface [64,65]. Figure 6(a) shows schematic diagrams of the (001) crystal plane for cubic-phase LSCF-*Pm*3*m*, cubic-phase HELSCF-*Pm*3*m*, and orthorhombic-phase HELSCF-*Pbnm*. As shown in Fig. 6(b), the adsorption energies of O at the Co and Fe sites of HELSCF-*Pbnm* are −1.17 and −1.67 eV, respectively,

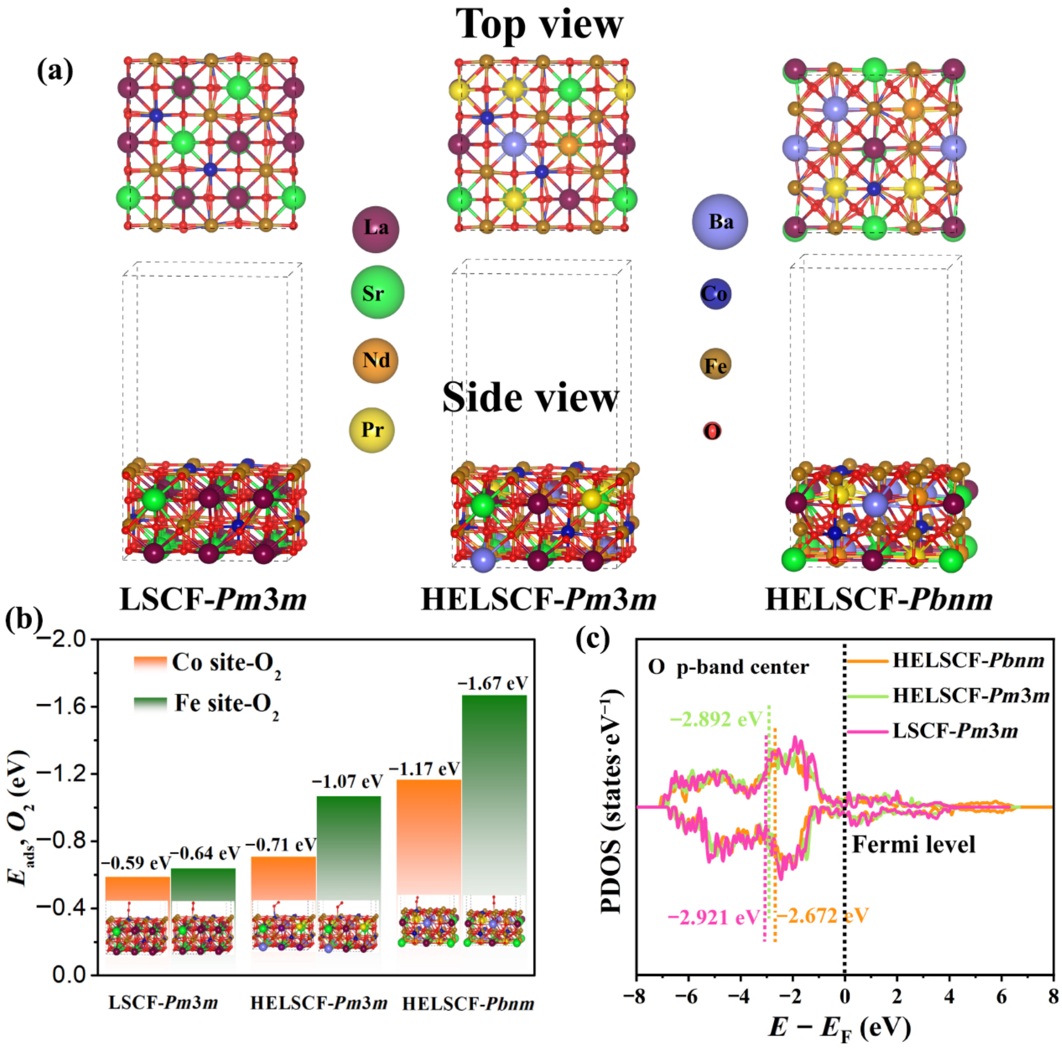

Fig. 6 (a) Top and side views of the (001) crystal plane for LSCF-*Pm*3*m*, HELSCF-*Pm*3*m*, and HELSCF-*Pbnm*. (b) Energy level diagrams of O_2 adsorbed on the Co and Fe surfaces of all electrodes (the inset shows the adsorption behavior of O_2 on the surface Co and Fe sites). (c) Partial density of states of all electrodes.

which are lower than those of HELSCF-*Pm*3*m* (−0.71 and −1.07 eV) and LSCF-*Pm*3*m* (−0.59 and −0.64 eV). By comparing HELSCF-*Pm*3*m* and LSCF-*Pm*3*m*, it can be seen that the high-entropy effect facilitates the adsorption of O_2 molecules on the surfaces terminated with CoO_2 and FeO_2 structures. Meanwhile, the asymmetric orthorhombic HELSCF-*Pbnm* induces extensive lattice distortion, which further reduces the energy barrier for O_2 adsorption on the surfaces terminated with CoO_2 and FeO_2 structures [65]. Figure 6(c) shows the partial density of states (PDOS) of the three electrodes. The O 2p-band center is generally regarded as a key indicator for describing the ORR activity of electrodes, and the dashed line represents the Fermi level. The calculated O 2p-band centers of HELSCF-*Pbnm*, HELSCF-*Pm*3*m*, and LSCF-*Pm*3*m* are −0.267, −0.289, and −0.291 eV, respectively. The higher O 2p-band center of HELSCF-*Pbnm* is closer to the Fermi level, indicating stronger hybridization with the 3d orbitals of transition metals. The optimized electronic structure is conducive to improving the ORR and OER performance [66].

In addition, to better understand lattice distortion and its impact on electrocatalytic activity, the structural comparative analysis process (SCAP) can be employed to quantify distortions, which are classified into external distortions (EDs) and internal distortions (IDs) [67]. Specifically, EDs result from continuous tilting and rotation between unit crystals induced by symmetry, while IDs are mainly caused by slight changes in bond lengths and bond angles triggered by atomic doping [68]. Combined with the XRD data refinement results and distortion degree analysis, with cubic-phase LSCF-*Pm*3*m* as the reference, the low distortion degree of HELSCF-*Pm*3*m* is dominated by internal distortions, primarily arising from the high-entropy effect induced by multiatomic doping. In contrast, HELSCF-*Pbnm* also possesses a high-entropy effect, thus exhibiting not only internal distortions but also irregular tilting and rotation caused by external distortions from the asymmetric structure. These factors further lengthen the bond lengths between oxygen atoms and B-site atoms. Therefore, even among high-entropy LSCFs with the same atomic composition, the internal distortion effect of HELSCF-*Pbnm* is further enhanced. Consequently, the strategy proposed in this study, without altering the ABO_3-type perovskite structure, maximizes the distortion degree of ABO_3-type perovskites through the combination of crystal asymmetry and high-entropy structure. Additionally, oxygen vacancies are the main factor directly affecting electrocatalytic activity, and the B-sites of ABO_3 perovskites are the primary locations for oxygen vacancy formation. Since the B-site atoms of the three electrodes are identical, the increase in B–O bond lengths and the deviation of bond angles enhance the oxygen vacancy formation capacity. Combined with the results of XPS, EPR, and electrocatalytic experiments, as well as the verification by DFT calculations, it is confirmed that the high-entropy HELSCF-*Pbnm* dominated by high external distortions exhibits the strongest electrocatalytic activity.

3.4 CO_2 tolerance analysis

In addition, considering that electrode materials containing alkaline earth metals are prone to CO_2 poisoning, this study also investigated the CO_2 tolerance of LSCF-*Pm*3*m* and HELSCF-*Pbnm* [27]. Figure S18 in the ESM presents the XPS spectra characterizing the chemical environments of alkaline earth metal ions (Ba^{2+} and Sr^{2+}) in LSCF-*Pm*3*m* and HELSCF-*Pbnm*. Considering the elemental stoichiometric ratios of the two materials, the total content of alkaline earth metal ions in LSCF-*Pm*3*m* is equal to that in HELSCF-*Pbnm*, following the relationship $\mathrm{Sr}_{\text{LSCF-}Pm3m} = \mathrm{Sr}_{\text{HELSCF-}Pbnm} + \mathrm{Ba}_{\text{HELSCF-}Pbnm}$. Quantitative conversion shows that the surface content of alkaline earth metals in HELSCF-*Pbnm* is 44.78%, which is lower than the 54.25% detected in LSCF-*Pm*3*m*. Previous studies [11] have demonstrated that, from a thermodynamic perspective, high configurational entropy can raise the free energy barrier for cation migration toward the surface, alter segregation pathways, and reduce the driving force for surface enrichment. From a structural mechanism perspective, high-entropy materials stabilize defect structures via the so-called “sluggish diffusion effect”, which maintains the continuity of active sites in the triple-phase boundary region. Meanwhile, they construct a cation migration state with high barriers and low mobility at the lattice level, significantly slowing down the kinetics of cation segregation and surface reconstruction. Consequently, HELSCF-*Pbnm* with a high-entropy structure can suppress the segregation of alkaline earth metal cations such as Ba^{2+} and Sr^{2+} compared to LSCF-*Pm*3*m*, which is consistent with previous reports [9,14]. Figures 7(a) and 7(b) show the EIS curves and ASR variation curves of the symmetric cells based on LSCF-*Pm*3*m* and HELSCF-*Pbnm*, respectively, under different CO_2 concentrations. As seen from the EIS and ASR curves, the variation range of the ASR value of LSCF-*Pm*3*m* with increasing CO_2 concentration is higher than that of HELSCF-*Pbnm*. At a CO_2 concentration of 10%, the ASR value of LSCF-*Pm*3*m* decreases from the initial 0.270 to 0.367 $\Omega\cdot cm^2$ (recession rate: 35.9%), while that of HELSCF-*Pbnm* decreases from the initial 0.074 to 0.083 $\Omega\cdot cm^2$ (recession rate: 12.7%). In addition, after the CO_2 tolerance test, the ASR of LSCF-*Pm*3*m* recovers to 0.294 $\Omega\cdot cm^2$, and that of HELSCF-*Pbnm* can reach 0.076 $\Omega\cdot cm^2$. Figure S19 in the ESM shows the degradation rates of ASR for LSCF-*Pm*3*m* and HELSCF-*Pbnm* after treatment with different CO_2 concentrations. It can thus be concluded that HELSCF-*Pbnm* has less carbonate deposition on its surface and exhibits superior CO_2 tolerance. The enhanced CO_2 tolerance of HELSCF-*Pbnm* can be explained from two aspects. First, the high-entropy structure itself can inhibit the segregation of alkaline earth metal cations. In combination with the fact that the A-site cations selected for high entropy in this study possess higher acidity in the order of $Nd^{3+} > Pr^{3+} > Sr^{2+} > Ba^{2+} > La^{3+}$ [69], they further help suppress the formation of carbonates on the electrode surface. These two mechanisms together contribute to the excellent CO_2 tolerance exhibited by HELSCF-*Pbnm*. Figure 7(c) shows the DRT curves corresponding to the EIS of LSCF-*Pm*3*m* and HELSCF-*Pbnm* in the CO_2 tolerance test. It can be observed that LSCF-*Pm*3*m* undergoes overall degradation under a CO_2 atmosphere, mainly due to the segregation of alkaline earth metal ions to form carbonates, which hinders the contact between oxygen and ORR active sites and impairs the charge transfer capability. The degradation of HELSCF-*Pbnm* is mainly caused by oxygen ion diffusion and oxygen adsorption/dissociation, which can be attributed to the decreased p_{O_2} resulting from the increase in CO_2 content. To further verify the CO_2 tolerance of the electrode materials, Figs. 7(d) and 7(e) show the FT-IR curves and XRD patterns of the electrode powders after treatment at 700 °C under a 5% CO_2 atmosphere, respectively. The carbonate content of HELSCF-*Pbnm* is significantly lower than that of LSCF-*Pm*3*m*, which further confirms its excellent CO_2 tolerance. Figure 7(f) is the reaction mechanism diagram of LSCF-*Pm*3*m* and HELSCF-*Pbnm* as SOC electrodes under a CO_2 atmosphere.

4 Conclusions

Based on the traditional LSCF perovskite, this study prepared SOC electrode materials with HEP. The research found that HELSCF with different crystal structures can be obtained by

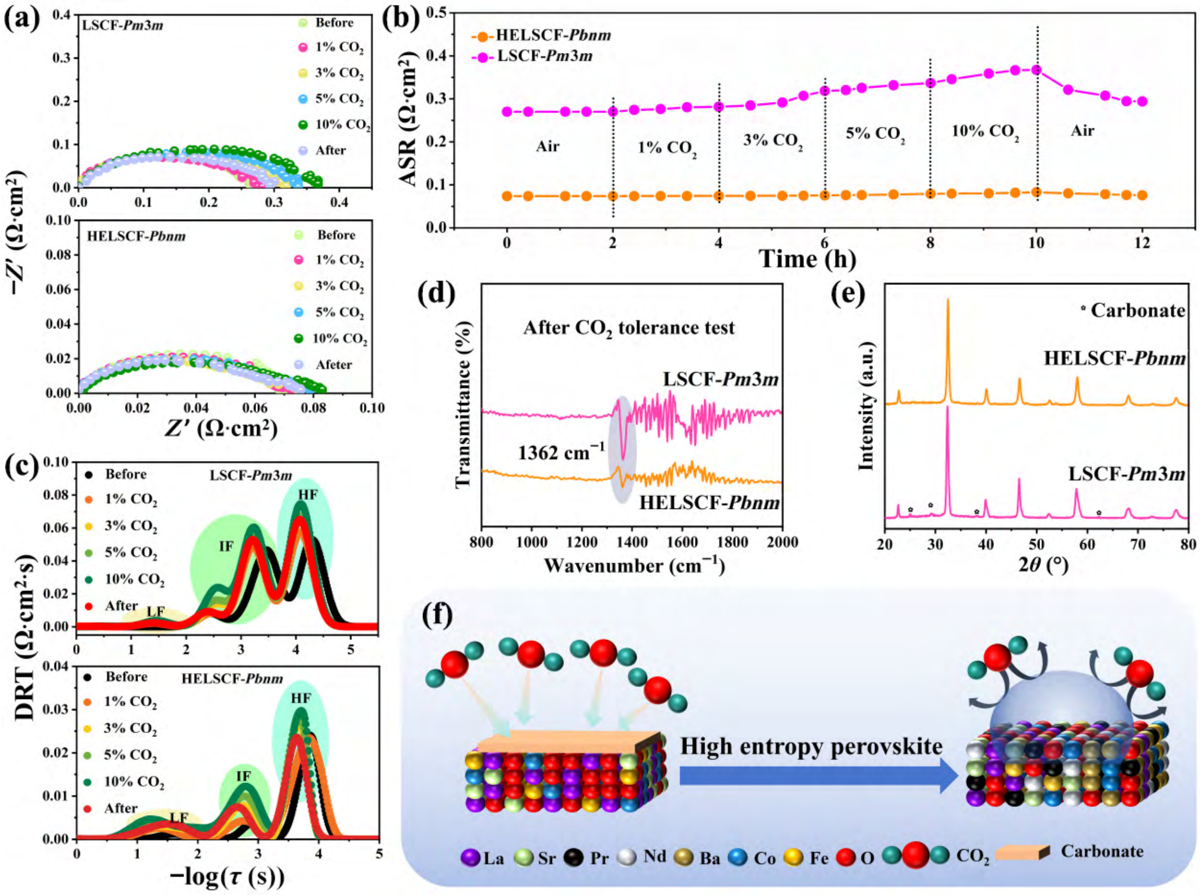

Fig. 7 (a) EIS curves of LSCF-*Pm*3*m* and HELSCF-*Pbnm* under different CO_2 concentrations at 700 °C and (b) CO_2 tolerance test curves; (c) DRT curves corresponding to the EIS curves in (a); (d) FT-IR and (e) XRD patterns of LSCF-*Pm*3*m* and HELSCF-*Pbnm* powders calcined at 700 °C in a CO_2 atmosphere for 10 h; (f) reaction mechanism diagrams of LSCF-*Pm*3*m* and HELSCF under a CO_2 atmosphere.

regulating the calcination temperature. The experimental results demonstrate that HELSCF-*Pbnm* with an asymmetric orthorhombic lattice structure exhibits a higher degree of lattice distortion, a greater concentration of oxygen vacancies, and an optimized electronic structure compared to HELSCF-*Pm*3*m* with a symmetric cubic lattice structure, which is conducive to enhancing the ORR and OER activities of the electrode. At 750 °C, when assembled as a symmetrical cell, HELSCF-*Pbnm* achieves an ASR value of 0.040 Ω·cm², which is lower than that of HELSCF-*Pm*3*m* (0.084 Ω·cm²) and LSCF-*Pm*3*m* (0.123 Ω·cm²). HELSCF-*Pbnm* also exhibits the highest exchange current density under the OER mode. When fabricated into the electrode of a single cell, it delivers an MPD of 1.38 W·cm⁻², which is 1.7 times that of the LSCF-*Pm*3*m*-based single cell. In addition, it shows excellent stability under both ORR and OER modes during long-term stability tests at 600 °C. DFT calculation results reveal that the oxygen vacancies generated by lattice distortion and the optimized electronic structure synergistically enable HELSCF-*Pbnm* with an asymmetric orthorhombic lattice structure to achieve optimal ORR and OER catalytic activities. Thus, HELSCF-*Pbnm* not only displays excellent oxygen reduction reaction activity but also has the potential to serve as a high-efficiency oxygen evolution reaction catalyst. Lowering the calcination temperature suppresses grain coarsening at the electrode morphology level, thereby increasing the active surface area for catalytic reactions. At the crystal structure level, it enables the formation of an asymmetric orthorhombic lattice with a high oxygen vacancy concentration and a favorable electronic structure. Synergistically improved from both structural and morphological perspectives, the electrocatalytic activity of the material is significantly enhanced, offering a simpler and more efficient strategy for the preparation of high-performance SOC electrodes. However, this work still has certain limitations and challenges. For instance, whether the high-entropy strategy combined with temperature modulation can be applied to Ruddlesden−Popper phase perovskites, double perovskites and spinel oxide systems remains a key issue worthy of in-depth investigation in future research.

Acknowledgments

This work was supported by the Jilin Provincial Education Department Foundation (Grant No. JJKH20261303KJ), the National Natural Science Foundation of China (Grant No. 22479072), and the Open Foundation of State Key Laboratory of Inorganic Synthesis and Preparative Chemistry (Grant No. 2024-15).

Availability of data and materials

The data that support the findings of this study are available from the corresponding author upon reasonable request.

Competing interests

The authors have no competing interests to declare that are relevant to the content of this article.

Electronic Supplementary Material

Supplementary material is available in the online version of this article at https://doi.org/10.26599/JAC.2026.9221315.

References

[1] Duan Y, Li H, Li S, *et al.* Thermal expansion matching as a key criterion for developing high-performance Mn-based mullite cathodes in SOFCs. *Adv Mater* 2026, **38**: 13615.

[2] Liu X, Huang L, Xi X, *et al.* Regulating the d–p orbital hybridization in $BaCo_{0.4}Fe_{0.4}Zr_{0.1}Y_{0.1}O_{3-\delta}$ via Cu doping for high-performance solid oxide fuel cells cathode. *Chem Eng J* 2025, **513**: 162958.

[3] Chen Y, Zhu J, Xia T, *et al.* Improved electrocatalytic activity and CO_2 tolerance of iron-based perovskite as an intermediate temperature SOFC cathode. *Fuel* 2024, **375**: 132546.

[4] Wan B, Liu T, Chang Y, *et al.* Thermodynamic NiO exsolution for durable and efficient cobalt-free cathodes in proton-conducting solid oxide fuel cells. *J Adv Ceram* 2026, **15**: 9221199.

[5] Chen Y, Chen Y, Ding D, *et al.* A robust and active hybrid catalyst for facile oxygen reduction in solid oxide fuel cells. *Energy Environ Sci* 2017, **10**: 964–971.

[6] Bai J, Niu L, Zhu Q, *et al.* Ni-doped Fe-based perovskite to obtain multifunctional and highly efficient electrocatalytic active IT-SOFC electrode. *Fuel* 2024, **365**: 131334.

[7] Gao J, Li Q, Xia W, *et al.* Advanced electrochemical performance and CO_2 tolerance of $Bi_{0.5}Sr_{0.5}Fe_{1-x}Ti_xO_{3-\delta}$ perovskite materials as oxygen reduction cathodes for intermediate-temperature solid oxide fuel cells. *ACS Sustainable Chem Eng* 2019, **7**: 18647–18656.

[8] Han X, Yang Y, Fan Y, *et al.* New approach to enhance Sr-free cathode performance by high-entropy multi-component transition metal coupling. *Ceram Int* 2021, **47**: 17383–17390.

[9] Han X, Li K, Shao Q, *et al.* A durable and highly active oxygen electrode for solid oxide cells: New insight into segregation suppression of layered perovskite. *Adv Mater* 2025, **37**: 2502068.

[10] Zhang D, Luo Y, Liu T, *et al.* Potential reduction-induced fast exsolution of hyperfine nanoparticles afford highly active CO_2 reduction reaction. *Appl Catal B Environ Energy* 2026, **382**: 125937.

[11] Xiao M, Di H, Liu Z, *et al.* High-entropy strategies transforming solid oxide cells: Progress and perspectives. *Mater Rep Energy* 2026, **6**: 100400.

[12] Gu Y, Shi J, Nematov D, *et al.* A brief review of high-entropy oxides in solid oxide fuel cell applications. *Mater Sci Eng B* 2026, **327**: 119260.

[13] Zou G, Liu H, Liu T, *et al.* High-entropy-induced CoO_6 octahedral distortion for boosted oxygen evolution reaction at high temperature. *Energy Environ Sci* 2025, **18**: 9478–9489.

[14] Yao C, Liu W, Zhang H, *et al.* High-entropy perovskite $(Pr_{1/6}Nd_{1/6}Sm_{1/6}Ba_{1/6}Sr_{1/6})_{6/7}(Mn_{1/6}Co)_{6/7}O_{3-\delta}$ as a highly active and CO_2 durable cathode for solid oxide fuel cells. *Appl Catal B Environ Energy* 2025, **363**: 124789.

[15] Yao Y, Feng J, Xu L, *et al.* *In situ* construction of a high-entropy perovskite based tri-phase composite electrode toward efficient reversible solid oxide cells. *Adv Mater* 2025, **37**: 12257.

[16] Li Z, Guan B, Xia F, *et al.* High-entropy perovskite as a high-performing chromium-tolerant cathode for solid oxide fuel cells. *ACS Appl Mater Interfaces* 2022, **14**: 24363–24373.

[17] Weng Z, Liu L, Hu Y, *et al.* Significance of engineering the MnO_6 octahedral units to promote the oxygen reduction reaction of perovskite oxides. *Adv Mater* 2024, **36**: 2311102.

[18] Yang Y, Bao H, Ni H, *et al.* A novel facile strategy to suppress Sr segregation for high-entropy stabilized $La_{0.8}Sr_{0.2}MnO_{3-\delta}$ cathode. *J Power Sources* 2021, **482**: 228959.

[19] Zhang W, Ma W, Gao Y, *et al.* Small-size atom-driven distortion realizes high-entropy oxides with simultaneous chemical stability and activity enhancement enabling a practical cathode for solid oxide fuel cells. *Appl Catal B Environ Energy* 2026, **383**: 126147.

[20] Xu H, Dang L, Yan J, *et al.* A new $(La_{0.2}Nd_{0.2}Gd_{0.2}Sr_{0.2}Ba_{0.2})Co_{0.2}Fe_{0.8}O_{3-\delta}$ high-entropy oxide cathode for intermediate temperature solid oxide fuel cell. *Solid State Ion* 2023, **397**: 116233.

[21] Bai J, Han Z, Lv B, *et al.* Preparation of 3D structure high performance $Ba_{0.5}Sr_{0.5}Fe_{0.8}Cu_{0.2}O_{3-\delta}$ nanofiber SOFC cathode material by low-temperature calcination method. *Int J Hydrog Energy* 2021, **46**: 8132–8142.

[22] He B, Lai Z, Wang D, *et al.* MCTSGT: A graph theory-based Monte Carlo tree strategy for configuration search in disordered structures. *Acta Mater* 2026, **302**: 121628.

[23] Zhou Y, Hu X, Zhang W, *et al.* Breaking the activity-stability trade-off with a high-entropy perovskite oxygen electrode for sustainable solid oxide cells. *Joule* 2025, **9**: 102198.

[24] Wang H, Zhang W, Meng J, *et al.* Effectively promoting activity and stability of a $MnCo_2O_4$-based cathode by *in situ* constructed heterointerfaces for solid oxide fuel cells. *ACS Appl Mater Interfaces* 2021, **13**: 24329–24340.

[25] Zhang Y, Zhou D, Zhu X, *et al.* Preparation of Pr, Co Co-doped $BaFeO_{3-\delta}$-based nanofiber cathode materials by electrospinning. *Int J Hydrog Energy* 2024, **50**: 992–1003.

[26] Wang H, Zhang X, Zhang W, *et al.* Enhancing catalysis activity of $La_{0.6}Sr_{0.4}Co_{0.8}Fe_{0.2}O_{3-\delta}$ cathode for solid oxide fuel cell by a facile and efficient impregnation process. *Int J Hydrog Energy* 2019, **44**: 13757–13767.

[27] Jin F, Liu X, Niu B, *et al.* A new highly active and CO_2-stable heterostructure cathode material for solid oxide fuel cells developed from bismuth ion-modified cation-deficient $Nd_{0.9}BaCo_2O_{5+\delta}$. *Appl Catal B Environ Energy* 2024, **358**: 124410.

[28] Jia Y, Chen S, Shao X, *et al.* Synergetic effect of lattice distortion and oxygen vacancies on high-rate lithium–ion storage in high-entropy perovskite oxides. *J Adv Ceram* 2023, **12**: 1214–1227.

[29] Bai J, Zhou D, Niu L, *et al.* Preparation of high-performance multiphase heterostructures IT-SOFC cathode materials by Pr-induced *in situ* assembly. *Appl Catal B Environ Energy* 2024, **355**: 124174.

[30] Zhong F, Wang X, Wang L, *et al.* Tuning geometry distortion of pyrochlore $RE_2Zr_{1.95}Ni_{0.05}O_{7+\delta}$ anodes with rich oxygen vacancies for ammonia-fed solid oxide fuel cell. *Sep Purif Technol* 2023, **312**: 123397.

[31] Ji Q, Bi L, Zhang J, *et al.* The role of oxygen vacancies of ABO_3 perovskite oxides in the oxygen reduction reaction. *Energy Environ Sci* 2020, **13**: 1408–1428.

[32] Zhang W, Zhang L, Guan K, *et al.* Effective promotion of oxygen reduction activity by rare earth doping in simple perovskite cathodes for intermediate-temperature solid oxide fuel cells. *J Power Sources* 2020, **446**: 227360.

[33] Gong H, Zhou D, Zhu X, *et al.* Characterization of B-site Sc-doped $La_2Ni_{1-x}Sc_xO_{4+\delta}$ (x = 0, 0.05, 0.10, and 0.15) perovskites as cathode materials for IT-SOFCs. *Int J Hydrog Energy* 2024, **50**: 1492–1502.

[34] Liu C, Sun L, Li Q, *et al.* Doping effects of alkaline earth element on oxygen reduction property of high-entropy perovskite cathode for solid oxide fuel cells. *J Electroanal Chem* 2023, **941**: 117546.

[35] Lu F, Xia T, Li Q, *et al.* Heterostructured simple perovskite nanorod-decorated double perovskite cathode for solid oxide fuel cells: Highly catalytic activity, stability and CO_2-durability for oxygen reduction reaction. *Appl Catal B Environ* 2019, **249**: 19–31.

[36] Hu L, Zhou D, Zhu X, *et al.* A high-performance composite cathode based on thermal expansion complementation for SOFC. *Fuel* 2024, **362**: 130864.

[37] Fu M, Hu W, Tong H, *et al.* Sn-doped cobalt containing perovskite as the air electrode for highly active and durable reversible protonic ceramic electrochemical cells. *J Adv Ceram* 2024, **13**: 63–72.

[38] Luo Y, Zhang D, Liu T, *et al.* *In situ* exsolution of quaternary alloy nanoparticles for CO_2–CO mutual conversion using reversible solid oxide cells. *Adv Funct Mater* 2024, **34**: 2403922.

[39] Luo Y, Chang X, Wang J, *et al.* Precise regulation of *in situ* exsolution components of nanoparticles for constructing active interfaces toward carbon dioxide reduction. *ACS Nano* 2025, **19**: 1463–1477.

[40] Yu X, Ren R, Xu C, *et al.* Localized lattice strain in perovskite oxides for enhanced oxygen reduction reaction kinetics in solid oxide fuel cells. *Chem Eng J* 2025, **503**: 158541.

[41] ten Elshof JE, Lankhorst MHR, Bouwmeester HJM. Oxygen

exchange and diffusion coefficients of strontium-doped lanthanum ferrites by electrical conductivity relaxation. *J Electrochem Soc* 1997, **144**: 1060–1067.

[42] Yasuda I, Hikita T. Precise determination of the chemical diffusion coefficient of calcium-doped lanthanum chromites by means of electrical conductivity relaxation. *J Electrochem Soc* 1994, **141**: 1268–1273.

[43] Yasuda I, Hishinuma M. Electrical conductivity and chemical diffusion coefficient of strontium-doped lanthanum manganites. *J Solid State Chem* 1996, **123**: 382–390.

[44] Yu X, Wang Z, Ren R, *et al.* Heterovalent Cu^{2+}/Mo^{6+} bimetallic doping strategy for enhanced ORR kinetics and Cr tolerance in solid oxide fuel cell cathodes. *Chem Eng J* 2025, **524**: 168891.

[45] Zhang X, Wang C, Liu K, *et al.* Significantly enhanced stability and activity of a perovskite oxygen electrode for reversible protonic ceramic electrochemical cells by heterointerface engineering. *J Adv Ceram* 2025, **14**: 9221108.

[46] Han X, Ling Y, Yang Y, *et al.* Utilizing high entropy effects for developing chromium-tolerance cobalt-free cathode for solid oxide fuel cells. *Adv Funct Mater* 2023, **33**: 2304728.

[47] Li L, Dong Z, Xia T, *et al.* A series of bifunctional ReBaCo$_2$O^{5+} perovskite catalysts towards intermediate-temperature oxygen reduction reaction and oxygen evolution reaction. *Chem Eng J* 2023, **468**: 143762.

[48] Yao C, Zhang Z, Zhang H, *et al.* Rapid oxygen atom capture on perovskite surface boosting the activity and durability of cathode for solid oxide fuel cells. *Chem Eng J* 2024, **497**: 154769.

[49] Gong X, Sun M, Zhou L, *et al.* RE-site high-entropy double perovskite La$_{0.2}$Pr$_{0.2}$Nd$_{0.2}$Sm$_{0.2}$Y$_{0.2}$BaCo$_2$O$_{5+\delta}$ as cathode material for solid oxide fuel cells. *Ceram Int* 2025, **51**: 53944–53952.

[50] Shang D, Zhang B, Zhang L, *et al.* Improving electrocatalytic activity through multi-element doping to A-site of Fe-based perovskite cathode for solid oxide fuel cells. *Chem Eng J* 2025, **506**: 160067.

[51] Yao C, Sun Y, Zhang H, *et al.* A highly active and durable iron-based high-entropy perovskite cathode for solid oxide fuel cells. *J Energy Chem* 2025, **110**: 558–570.

[52] Fu X, Lü S, Meng X, *et al.* High-entropy cobalt-free perovskite as a high-performing nanofiber cathode for solid oxide fuel cells. *J Mater Chem A* 2024, **12**: 27452–27463.

[53] Li R, Zhang J, Chen Z, *et al.* A stable high-entropy perovskite La$_{0.2}$Pr$_{0.2}$Nd$_{0.2}$Sm$_{0.2}$Sr$_{0.2}$Co$_{0.8}$Fe$_{0.2}$O$_{3-\delta}$ oxygen electrode for reversible solid oxide cells. *Mater Sci Eng B* 2025, **313**: 117857.

[54] Wang Y, Zhang X, Yang M, *et al.* A-site high entropy and B-site medium entropy double perovskite structure cathode material for solid oxide fuel cells. *J Alloys Compd* 2025, **1022**: 180002.

[55] Zielińska K, Dąbrowa J, Zajusz M, *et al.* Alkali free perovskites–Exploiting B-site synergies in Sr-free, high-entropy cathodes for intermediate-temperature Solid-Oxide fuel cells. *Chem Eng J* 2025, **504**: 158974.

[56] Li X, Feng J, Sun N, *et al.* A-site high-entropy engineering of oxygen electrode: A promising route to durable and active reversible solid oxide cells. *Adv Mater* 2026, **38**: 21863.

[57] Di M, Zhang H, Zhang Z, *et al.* High-entropy Mn-based double perovskite as a highly active and CO$_2$-resistant cathode for solid oxide fuel cells. *Fuel* 2025, **400**: 135754.

[58] Liu X, Xi X, Liao Y, *et al.* Deciphering the enhanced oxygen reduction reaction activity of PrBa$_{0.5}$Sr$_{0.5}$Co$_{1.5}$Fe$_{0.5}$O$_{5+\delta}$ via constructing negative thermal expansion offset for high-performance solid oxide fuel cell. *Appl Catal B Environ Energy* 2024, **359**: 124509.

[59] Yao C, Xia B, Zhang H, *et al.* Temperature-controlled *in-situ* construction of composition-tunable nanoparticle-decorated SOFC cathodes with enhanced oxygen reduction kinetics and CO$_2$ tolerance. *Compos Part B Eng* 2025, **288**: 111917.

[60] Chang Y, Liu T, Rao J, *et al.* Steam-induced surface reconstruction of air electrodes for reversible protonic ceramic electrochemical cells. *Adv Funct Mater* 2026, **36**: 17821.

[61] Zhang Y, Chen B, Guan D, *et al.* Thermal-expansion offset for high-performance fuel cell cathodes. *Nature* 2021, **591**: 246–251.

[62] Zhou J, Tang P, Bai JH, *et al.* A new type of Gd$_{0.2}$Ce$_{0.8}$O$_{3-\delta}$ fuel cell electrolyte containing Er$_{0.2}$Bi$_{0.8}$O$_{1.5}$ with highly improved performance. *J Alloys Compd* 2022, **901**: 163654.

[63] Shi S, Gao J, Liu Y, *et al.* Multi-scale computation methods: Their applications in lithium–ion battery research and development. *Chin Phys B* 2016, **25**: 018212.

[64] Gao J, Liu Y, Gao Y, *et al.* Cobalt-free fluorine doped Bi$_{0.7}$Sr$_{0.3}$FeO$_{3-\delta}$ oxides for energetic cathodes of low-temperature solid oxide fuel cells. *Chem Eng J* 2023, **452**: 139584.

[65] Liu D, Dou Y, Xia T, *et al.* B-site La, Ce, and Pr-doped Ba$_{0.5}$Sr$_{0.5}$Co$_{0.7}$Fe$_{0.3}$O$_{3-\delta}$ perovskite cathodes for intermediate-temperature solid oxide fuel cells: Effectively promoted oxygen reduction activity and operating stability. *J Power Sources* 2021, **494**: 229778.

[66] Zhang Y, Wang Y, Liu Z, *et al.* Constructing robust and efficient ceramic cells air electrodes through collaborative optimization bulk and surface phases. *Adv Funct Mater* 2025, **35**: 2422531.

[67] Fang C, Wang H, Shi S. Quantifying structural distortion manipulation for desired perovskite phase: Part I. *Paradigm demonstration in tungsten oxides. J Materiomics* 2024, **10**: 293–303.

[68] Fang C, Wang H, Shi S. Quantifying structural distortion manipulation for desired perovskite phase: Part II. *Three-step workflow to reveal phase evolution logic. J Materiomics* 2024, **10**: 304–314.

[69] Jeong N, Lee J, Tae E, *et al.* Acidity scale for metal oxides and Sanderson's electronegativities of lanthanide elements. *Angew Chem Int Ed* 2008, **47**: 10128–10132.